

www.acsanm.org Article

Self-Assembly of Nanoporous ZIF-8-Based Superstructures for Robust Chemical Sensing of Solvent Vapors

Zhihuan Li,[§] Li Feng,[§] Gaohang Huo, Jiayi Hao, Chen Li, Zhengze He, Evgeniya Sheremet, Yadong Xu, and Jianxi Liu*



Cite This: ACS Appl. Nano Mater. 2024, 7, 3479-3487



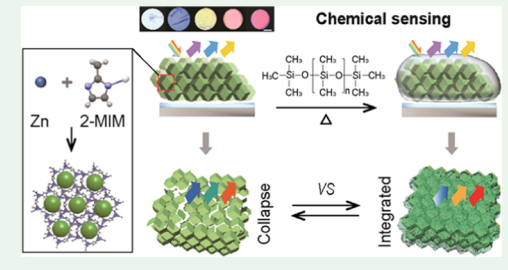
ACCESS I

III Metrics & More

Article Recommendations

Supporting Information

ABSTRACT: Self-assembly of metal—organic frameworks (MOFs) to construct optical sensors has been proposed to detect chemicals by acclimating colors in response to analytes that adsorbed on the surface of MOF nanoparticles and in the interspaces between particles. However, the instability of the weakly assembled optical structures held together by van der Waals forces limits their active sensing application. Here, we propose full-color tunable superstructures that are constructed by self-assembled ZIF-8 nanoparticles and postsynthetic poly-(dimethylsiloxane) (PDMS) coating, which behave as robust optical sensors. The optical band was tuned by controlling the size of the ZIF-8 particles and also responded to the adsorption of chemicals with different refractive indexes in the



micropores of the ZIF-8 particles. In addition, PDMS-coated ZIF-8 superstructures (ZIF-8@PDMS) were fabricated by thermal evaporation to optimize the optical quality and improve the robustness and solvent resistance during chemical sensing. Static and dynamic sensing results showed that the hierarchical porous structures endow the ZIF-8@PDMS superstructure with higher optical saturation and faster response in comparison to their counterparts configured with a ZIF-8 superstructure.

KEYWORDS: self-assemble, structure color, PDMS, ZIF-8, microporous materials

1. INTRODUCTION

Colorimetric chemical sensors offer a facile and inexpensive detection approach for portable or point-of-care settings that can be as accessible as detection by the naked eye. The key is applying structures with adjustable optical properties such as optical absorbers based on thin-film interference effects. They are widely used in the fields of photonic and chemical sensing,^{2,3} display technology,⁴ and solar cells⁵ due to their variable photonic band gap. Fabry-Pérot (F-P) optical sensors have been widely investigated for their fast response time, which is typically accomplished by detecting photonic band shifts caused by changes in the chemical composition of the environment. According to Bragg's law, the photonic band of an F-P sensor can be tuned by changing the effective refractive index and the spacing between the interference films. In the past few years, opal structure, 8 inverse opal structure,9 or gel film structure10 made of functional materials have been used to construct periodic structures with fascinating optical properties. Dynamic tuning of optical properties by adding some molecules 10 would provide a facile method for a plethora of chemical sensors, but it is difficult to apply them to distinguish different chemicals with a similar refractive index because they will cause the same photonic band shift. To overcome this problem, Kou et al.11 demonstrated the possibility of distinguishing between benzene, toluene, xylene, and ethylbenzene based on differences in the solvation behavior. In addition, Zhang et al. 12

developed a dynamic reflectance spectroscopy method based on the different diffusion behavior of solvent molecules in the inverse opal structure for chemical sensing. However, the mentioned methods are still relatively complex and do not allow one to establish a direct relationship between photonic band shift and molecular size. ^{13,14} Therefore, the realization of sensitive responses to molecular size and detection techniques to distinguish between chemicals with similar refractive indices remains challenging.

Metal—organic frameworks (MOFs) formed by orderly integration of metal ions/clusters and organic ligands are ideal candidates for selective sensing due to their high porosity that enhances the ability to absorb molecules, as well as control the pore properties and chemical environment. Several MOF-based optical sensors have been proposed to detect chemicals through the modulation of their reflectance response. To example, Liu et al. designed and synthesized monodisperse poly amidoamine (PAMAM) dendrimer-modified zeolitic imidazolate framework particles (PAMAM@ZIF-8) via a postsynthetic method, which can form homogeneous optical

Received: January 4, 2024 Revised: January 9, 2024 Accepted: January 10, 2024 Published: January 23, 2024





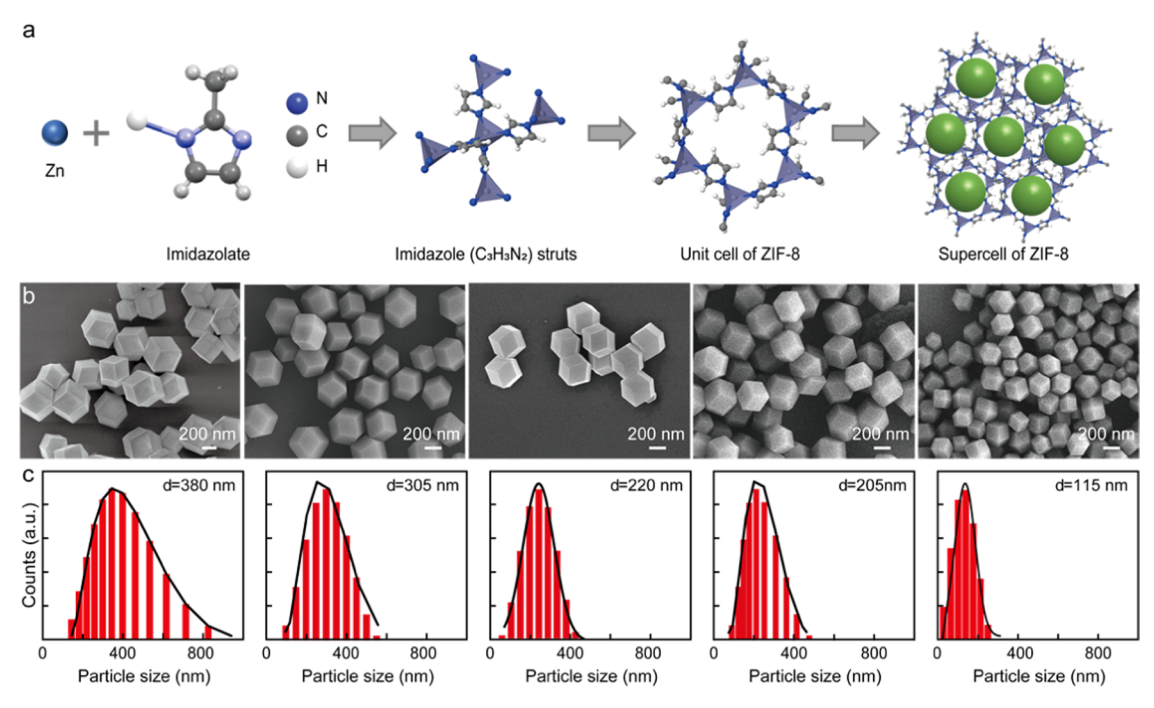


Figure 1. Morphology characterization and size distribution of monodispersed ZIF-8 particles. (a) Schematic illustration of the synthesis of ZIF-8 nanoparticles. (b) Representative field-emission scanning electron microscopy images of ZIF-8 particles of different sizes. (c) Size-distribution histograms of ZIF-8 particles of different sizes obtained by DLS: from left to right, mean particle sizes are d = 382 nm; d = 305 nm; d = 218 nm; d = 207 nm; d = 115 nm.

films with different structural colors. Zhang et al.²⁰ reported the preparation of MOF-based optical sensors with stable and tunable optical properties by assembling UiO-66 crystals with controllable size and missing linker defects. The sensor shows fast response (2.00 s) and short recovery time (3.00 s) to ethanol vapors, which demonstrates that the tunable microand mesostructural features of UiO-66 greatly contribute to the optimization of device performance. Detection sensitivity is improved, even for polycrystalline MOF nanoparticles. However, these methods fail to fully utilize the inherent porosity of MOFs because analytes are mainly adsorbed on the surface of MOF nanoparticles and in the interspaces between particles.²¹ Although high porosity could be obtained from selfassembled porous MOFs in a single layer, structural colors only appeared on the film after the assembly of multilayer MOFs.² Therefore, matching between visible band reflection and thickness of the film is difficult to satisfy in the construction of single-layer MOF nanoparticles for visual chemical sensing. If MOFs are prepared in the form of monodispersed nanocrystals and self-assembled into three-dimensional (3D) photonic superstructures, then the system can fully benefit not only from the chemical environment of the MOF pores but also from the well-defined microscale structure. Unfortunately, the instability of weakly assembled 3D photonic structures held together by van der Waals forces limits their application in device integration.

Herein, we present a robust superstructure with reflectivity tuned throughout the full optical range prepared by the self-assembly of monodisperse ZIF-8 nanocrystals capable of distinguishing chemicals with similar refractive indices. Colloidal crystalline polyhedral MOF particles were synthesized with precisely controlled size to subsequently self-assemble into well-ordered three-dimensional superstructures. The ZIF-8 superstructure color was tuned over a broad frequency range by adjusting the dimensions of MOF

nanocrystals. Robustness and solvent resistance of MOF-based superstructures were achieved by deposition of the nanoscale hydrophobic resin poly(dimethylsiloxane) (PDMS). Chemical sensing on the PDMS-coated ZIF-8 (ZIF-8@PDMS) superstructure shows breakthrough enhancement of responsivity compared to the pure ZIF-8 superstructure. Homogeneous encapsulation of functional small guest molecules in MOF films contributes to specific physical—chemical properties that benefit device applications in optical communication and chemical sensing. Our work not only provides a new way to fabricate MOF-based sensor materials but also extends their application in the field of device integration.

2. RESULTS AND DISCUSSION

2.1. Synthesis of Nanoporous ZIF-8 Particles. Figure 1 shows the synthesis of highly monodisperse colloidal truncated rhombic dodecahedral (TRD) ZIF-8 nanoparticles in water (SI, Methods). ZIF-8 is known to synthesize by linking imidazolate chains and the tetrahedral zinc center and gives rise to a sodalite (SOD) topology similar to that of silica polymorphs (Figure 1a), which allowed the structure of ZIF-8 to be dependent on the chemical properties of the bridged imidazolate units.²³ A SOD cage was defined as the primary unit cell of the ZIF-8 structure attached to eight identical apertures, which were then duplicated to generate 3D supercells. First, 2-methylimidazole (2-MIM) was protonated under the action of a solvent or heat and reacted with zinc ions to form the crystal nuclei of ZIF-8. Then, excessive neutral 2methylimidazole was adsorbed on the surface of positively charged ZIF-8 nanoparticles to stop the growth of ZIF-8.2 The size and morphology of ZIF-8 particles were regulated by introducing cetyltrimethylammonium bromide (CTAB) as a cationic surfactant and a capping agent. The first crystallites of

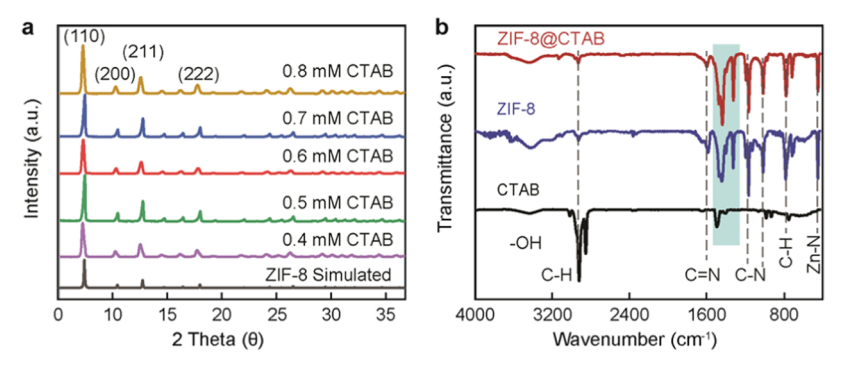


Figure 2. Synthesis of ZIF-8 particles stabilized by using CTAB as a cationic surfactant and a capping agent. (a) Simulated and synthesized PXRD patterns of ZIF-8 particles of different sizes. The morphology of ZIF-8 particles of different sizes synthesized by different concentrations of CTAB is similar, including (110), (200), (211), (222), and other truncated rhombohedron characteristic crystal planes. (b) FTIR of ZIF-8 particles.

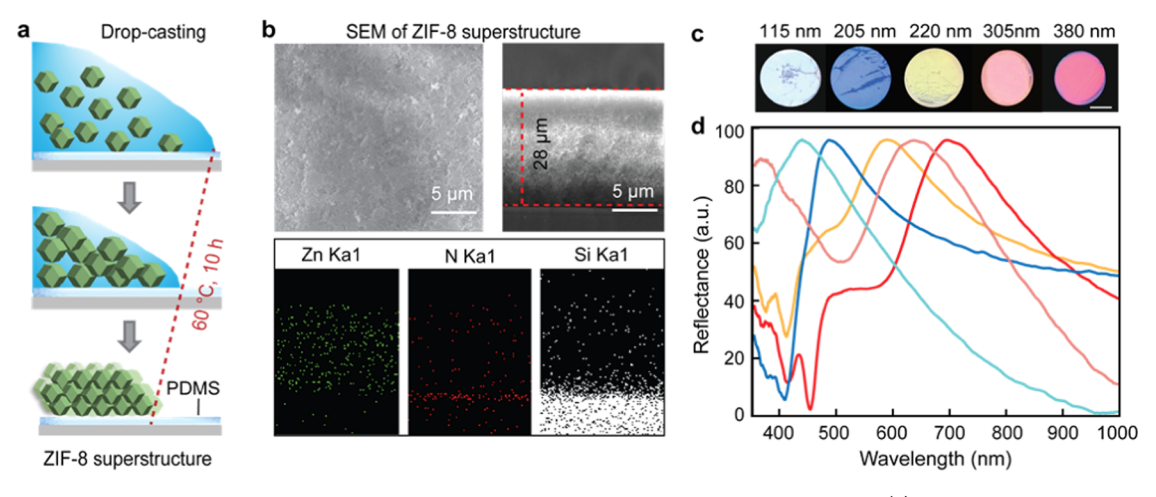


Figure 3. Tuning reflection band of the MOF-based F–P sensor self-assembled by ZIF-8 nanoparticles. (a) Schematic diagram of the assembly process of the superstructure. (b) SEM, cross-section SEM images, and EDS mapping of the self-assembled superstructure with an average ZIF-8 size of 308 nm. (c) Optical photographs and (d) normalized optical reflection spectra at incidence angle $\theta = 0^{\circ}$ of self-assembled ZIF-8 nanoparticles of different sizes: 115 nm (cyan); 207 nm (blue); 220 nm (yellow); 305 nm (pink); and 380 nm (red); the scale bar is 5 mm.

ZIF-8 were cubic-shaped seeds, which gradually evolved into TRD nanoparticles and RD nanoparticles due to the superior growth of the (100) plane.²⁵ So we can fabricate well-defined TRD ZIF-8 nanoparticles with sizes ranging from 115 to 380 nm by controlling the content of CTAB from 0.8 to 0.4 mM (Figures 1b and S1). We found the sizes of ZIF-8 nanoparticles measured by dynamic light scattering (DLS) were 380, 305, 220, 205, and 115 nm with a narrow size distribution when the contents of CTAB were 0.4, 0.5, 0.6, 0.7, and 0.8 mM, respectively (Figure 1c). The result showed the consistency between static size and dynamic size for the ZIF-8 particles with high monodispersity and uniformity, which demonstrated great potential in constructing optical sensors with different structural colors.

Figure 2a depicts the powder X-ray diffraction (PXRD) data of the as-synthesized ZIF-8 nanoparticles with different sizes. The (110), (200), (211), and (222) characteristic crystal faces were all present on the ZIF-8 nanoparticles, which indicated the formation of the crystalline ZIF-8 structure. Fourier transform infrared (FTIR) spectra of CTAB show a strong adsorption peak of 3000 cm⁻¹, which can be attributed to the C–H stretching vibration mode of methyl in the linker (Figure 2b). The adsorption peak at 1575 cm⁻¹ was defined as the C=N bond stretching in ZIF-8, while the peaks at 1465 and 1383 cm⁻¹ corresponded to the imidazole stretching pattern. The adsorption peak at 800 cm⁻¹ was defined as the out-of-plane

bend of the C–H bond stretching in ZIF-8. In addition, we found that the imidazole ring stretching vibration characteristic peak appeared at 1420 cm⁻¹ and the Zn–N vibration appeared at 421 cm⁻¹.^{27–30} Obviously, the absorption peaks of the hydrogen bond (N–H···N) and vibration absorption peaks of the N–H bond in the imidazole ring were not found at 2600 and 1843 cm⁻¹, which indicated that 2-MIM has been completely deprotonated.^{31,32}

2.2. Self-Assembly of the Nanoporous ZIF-8-Based **F–P Sensor.** The F–P optical sensor is self-assembled into millimeter-sized three-dimensional superstructures by controlling the contact angle between the TRD ZIF-8 colloidal dispersion and the substrate. Figure 3a shows a schematic diagram of the assembly of ZIF-8 nanoparticles. Briefly, we placed a droplet of an aqueous colloidal dispersion of the ZIF-8 particles (50 mg mL⁻¹) on a PDMS surface, and then the sample was incubated in an oven at 25, 60, and 100 °C for 10 h (SI, Methods and Figures S2 and S3). We found that the optical property of the resulting F-P photonic cavities was improved by increasing the temperature from 25 to 60 °C. However, the optical quality was degraded at a higher assembly temperature of 100 °C due to the disordered stacking caused by the faster evaporation. Notably, all of the particles in the droplet formed tightly packed aggregates, and the three-phase contact line of the droplet receded during the drying process, which provided a strong driving force to push the particles

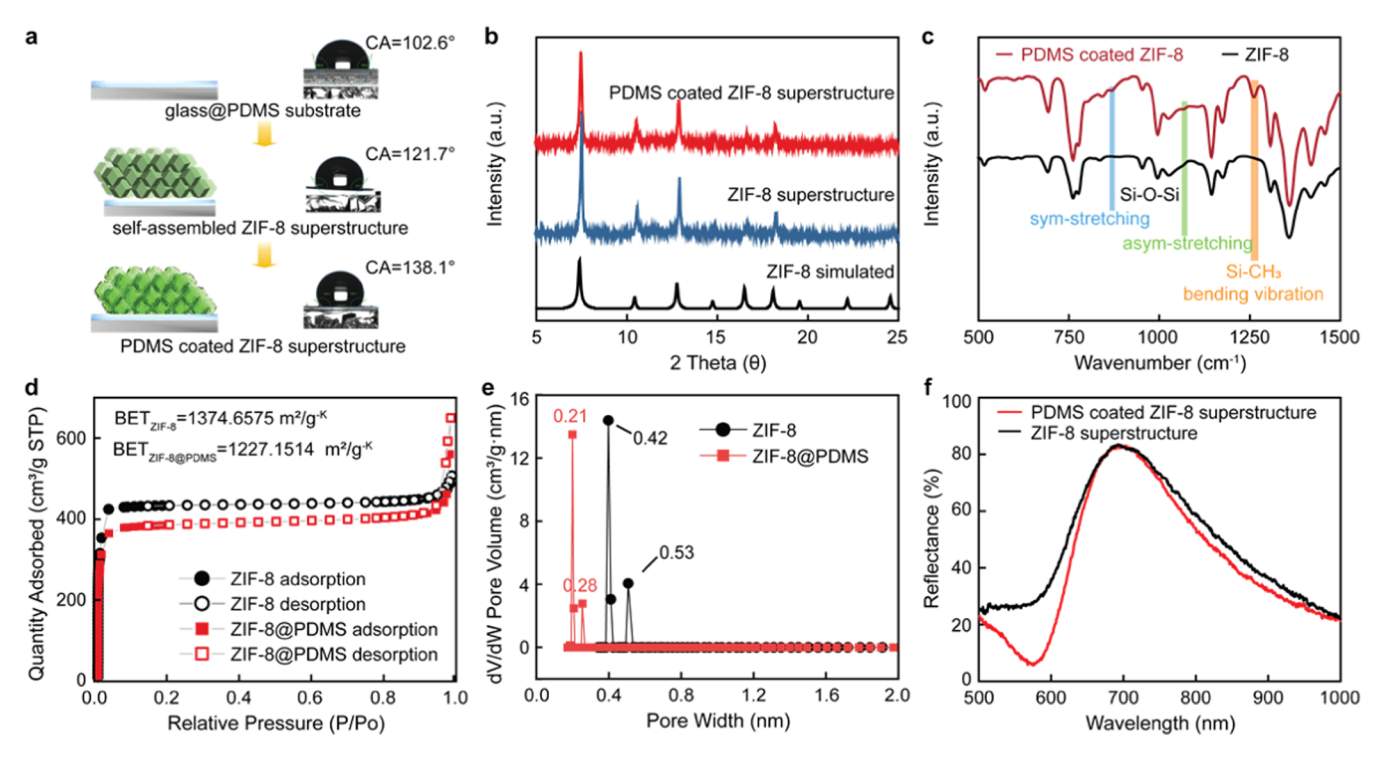


Figure 4. Physicochemical characterization of the PDMS-coated ZIF-8 superstructure with an average particle size of 380 nm. (a) Schematic diagram of the evaporative deposition of PDMS on the ZIF-8 superstructure surface and contact angles of water droplets on different films: top: glass@PDMS; middle: ZIF-8 superstructure; bottom: ZIF-8@PDMS superstructure. (b) PXRD and (c) FTIR spectra of the pristine ZIF-8 and ZIF-8@PDMS particles. (d) N_2 sorption isotherms and (e) pore size distribution of the pristine ZIF-8 and ZIF-8@PDMS particles. (f) Reflection spectra of the ZIF-8 and ZIF-8@PDMS superstructure.

inward for eliminating the coffee-ring effect and bringing about a dense assembly of ZIF-8 superstructures.³³

Figure 3b shows the close-up superstructure of selfassembled ZIF-8 nanoparticles with an average size of 308 nm, whose cross-section SEM images and EDS mapping demonstrated a homogeneous ordering of the three-dimensional structure. Figure 3c depicts the optical images of the ZIF-8 superstructures that are cyan, blue, yellow, pink, and red in color with nanoparticle sizes of 115, 207, 220, 305, and 380 nm, respectively. The corresponding reflection bands of the ZIF-8 superstructures were 450, 490, 600, 650, and 700 nm, which clearly demonstrated the consistency with visual structural colors (Figure 3d). A clear reflection band was observed, which was attributed to the opening of an optical band gap in the [001] direction in the reciprocal space. In addition, the reciprocal space was related to the Bragg-Snell reflection from (001) crystal planes of the ZIF-8 structure. In addition, close-up SEM images of the 207 nm ZIF-8 superstructure revealed a good arrangement of the nanocrystals (Figure S4). The TRD ZIF-8 particles mainly exhibited a facecentered cubic (FCC) crystal packing structure (Figure S5a), which was predominantly attributed to the absence of preferential facet-to-facet interactions between adjacent TRD ZIF-8 particles. 34,35 Hence, the inherent anisotropy of the TRD ZIF-8-based superstructure packed with FCC induced minimal discernible interstitial space between the particles within each layer. In contrast to the TRD ZIF-8-based superstructure, the nanosphere ZIF-8-based superstructure (Figure S5b) predominantly exhibited a hexagonal packed arrangement with various orientations, and their structure color was derived from thin-film interference rather than from Bragg diffraction of the scattered light from each particle. The

reason was attributed to the anisotropy and lack of periodic arrangement of the particles, which led to destructive interference of the scattered light from each particle to affect the optical quality of the structure. In addition, we found that the initial evaporation at room temperature yielded three-dimensional ordering but led to heterogeneity in the film thickness by generating thick surrounding walls around the droplet, which were formed by a "coffee ring" over time. A small number of defects unavoidably appeared due to lattice disordering; however, such defects do not deteriorate resonant reflectivity of the ZIF-8 superstructure. Overall, the optical properties of the resulting F–P sensor could be tuned by tailoring the size of the ZIF-8 building blocks.

2.3. PDMS Deposition of the Surface of the ZIF-8 Superstructure Photonic Cavity. To improve the robustness and the solvent resistance of the self-assembled MOFbased F-P sensor, we modified the surface of ZIF-8 by coating a protective layer of PDMS, which was permeable to vapors. The modification process includes a PDMS coating and curing. The coating of the PDMS layer on ZIF-8 is simply realized by heating a certain amount of PDMS with a self-assembled ZIF-8 superstructure in an oven at 235 °C in the presence of a PDMS stamp for 30 min and allowing it to cool to room temperature (Figure 4a). The long chain of PDMS can effectively prevent water molecules from being adsorbed into the internal pores of the self-assembled superstructure to improve their stability while retaining the inherent properties (i.e., high surface area, pore structure, and crystal structure) of ZIF-8.36 We studied the water contact angle (CA) of the PDMS substrate, the selfassembled ZIF-8 superstructure, and the PDMS-coated ZIF-8 superstructure (ZIF-8@PDMS) samples. The surface of the ZIF-8 superstructure was hydrophobic because the ligand had

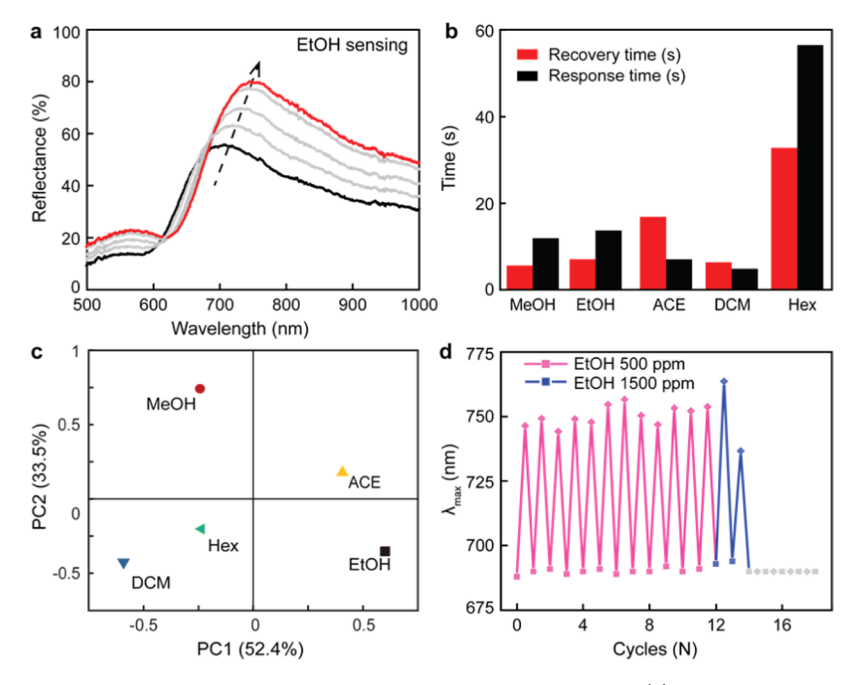


Figure 5. Chemical sensing properties of ZIF-8 superstructures with an MOF size of 380 nm. (a) Sensing performance of ZIF-8 superstructures over time upon exposure to ethanol vapor in comparison to pure nitrogen. (b) Dynamic behavior of the ZIF-8 superstructure upon exposure to various chemical vapors. (c) PCA plots for the ZIF-8 superstructure, illustrating the individual discrimination capability toward pure solvent vapors (methanol, ethanol, acetone, dichloromethane, and *n*-hexane). (d) Fourteen cycles of recoverable chemical sensing on the ZIF-8 superstructure.

an imidazole ring hydrophobic group. After coating of hydrophobic PDMS on the surface of the ZIF-8 superstructure, the water contact angle increased even further from 121.7 to 138.1°, which confirmed the surface properties were successfully modified by depositing PDMS coatings. PXRD patterns showed that the (110), (200), (211), and (222) crystal faces were all present on the ZIF-8@PDMS nanoparticles, which indicated that their crystal structure had no change in the diffraction peak position compared with the experiment and the simulated ZIF-8 superstructure (Figure 4b). Figure 4c depicts the FTIR spectra of the ZIF-8 superstructure before and after PDMS coating. Symmetric and antisymmetric stretching vibrational absorption peaks of Si-O-Si and methyl symmetric bending absorption peaks of Si-CH₃ were observed at 798.8, 1067.9, and 1259.0 cm⁻¹, respectively (Figure S6). The results indicated that PDMS was grafted successfully on ZIF-8.³⁷ In addition, the Brunner-Emmet-Teller (BET) surface areas of the pristine and PDMScoated ZIF-8 were calculated to be 1374.7 and 1227.1 m² g, respectively (Figure 4d). Meanwhile, the average pore diameter of ZIF-8 (0.53/0.42) was larger than that of ZIF-8@PMDS particles (0.28/0.21), which suggested that the inherent porous structure did not collapse after the PDMS coating (Figure 4e). Figure 4f shows the reflection spectrum changes of the ZIF-8 superstructure before and after the evaporative deposition of PDMS. The reflection band of the ZIF-8 superstructure appeared at $\lambda = 700$ nm with a full width at half-maximum of 200 nm. After evaporative deposition of PDMS, the reflection band of the ZIF-8@PDMS superstructure remained unchanged, and the full width at halfmaximum narrowed to 180 nm, which indicated the enhancement of naked-eye saturation and the tone of structure color.

2.4. Chemical Sensing Performance of the ZIF-8 Superstructure. Microporosity of the MOF is highly favorable for the development of ZIF-8 superstructures for

sensing applications since adsorption of chemicals in the MOF pores can change their refractive index, which allows a significant shift in the reflection band. To demonstrate the function of well-defined superstructures in promoting chemical sensing, we introduced the chemical vapors of analytes to the self-assembled ZIF-8 superstructure. Figure 5a shows reflection spectra of the ZIF-8 superstructure with a size of 380 nm during the ethanol (EtOH) sensing process. The saturated EtOH vapor was introduced into the cavity fixed inside a home-built flow cell. The primary reflection band at $\lambda = 700$ nm experienced a red-shift to 744 nm within 10 s after exposure to 500 ppm ethanol vapors. The large wavelength shift (44 nm) demonstrated high sensitivity of the superstructure. In addition, we conducted sensing of methanol (MeOH), acetone (ACE), dichloromethane (DCM), and nhexane (Hex) on the superstructure, which showed significant reflection band shifts of 47, 40, 50, and 49 nm, respectively (Figure S7). Figure 5b shows the difference in sensing response time and recovery time of the ZIF-8 superstructure calculated from time-resolved mean band reflections recorded interval per 0.5 s through exposure to different chemicals. When N₂ flows through the ZIF-8 superstructure, the reflection intensity remains constant. However, when the chemical vapor passes through, the reflection intensity changes significantly and then returns to the same level. The response time of the platform is defined as the differential reflectance when the signal reaches 95% of the maximum reflectance.³⁸ The response times of methanol, ethanol, acetone, dichloromethane, and n-hexane sensing were 5.9, 7.1, 18.6, 5.6, and 32.9 s, respectively. The corresponding recovery times were 12.9, 13.7, 7.0, 4.8, and 56.8 s, respectively. We found that *n*hexane possesses a higher response time and recovery time as compared to methanol, ethanol dichloromethane, etc. This phenomenon could be explained by the comparative low polarity of hexane.³⁹ In addition, we found an inconsistence

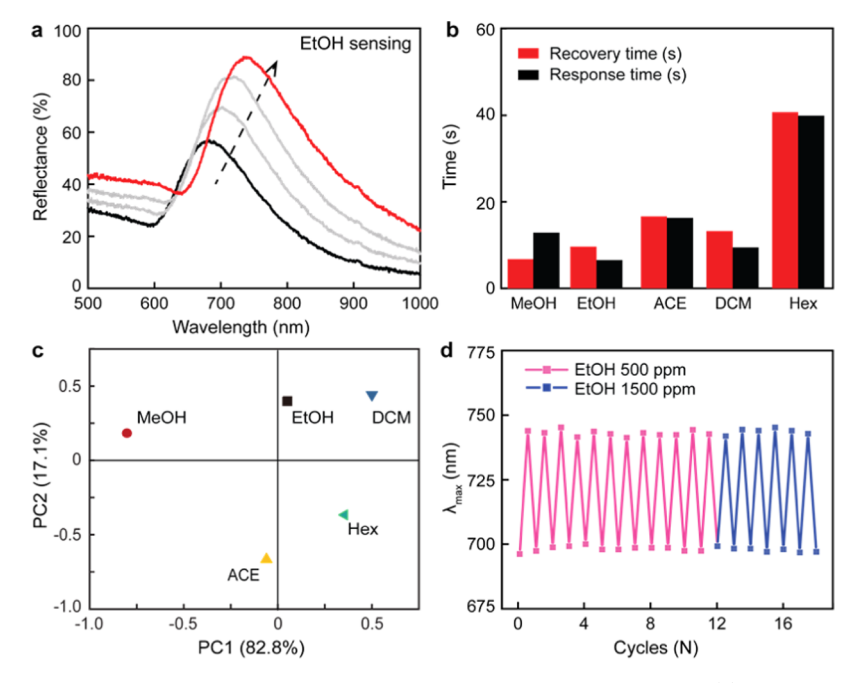


Figure 6. Chemical sensing properties of ZIF-8@PDMS superstructures with an MOF size of 380 nm. (a) Sensing performance of ZIF-8@PDMS superstructures over time upon exposure to ethanol vapor in comparison to pure nitrogen (black curve). (b) Dynamic behavior of ZIF-8@PDMS superstructures upon exposure to various chemical vapors. (c) PCA plots for ZIF-8@PDMS superstructures, illustrating the individual discrimination capability toward pure solvent vapors (methanol, ethanol, acetone, dichloromethane, and *n*-hexane). (d) Recoverable chemical sensing on the ZIF-8 superstructure for 18-repeating cycles.

between the response time and recovery times of the MOF-based sensors, which was attributed to the fact that adsorption and desorption of gas in MOFs are related to the pore size of MOFs, the diffusion coefficients of the gas, and the host—guest interactions between MOFs and gas molecules. 40,41

To characterize the ability of the ZIF-8 superstructure to separate different analyte vapors, we performed principal component analysis (PCA) that was calculated by the characteristic sensing data of each organic molecule, namely, refractive index, reflection band shift, and reflectance shift (ΔR) (Table S1). A 2D projection of the factor scores was calculated for each analyte, whereas the first and second principal components (PC1 and PC2) accounted for the most significant variance of the measurements (Figure 5c). We found a clear separation of all six chemicals on the cavity, which indicated high sensitivity for discrimination of the analytes because these points are scattered in different areas and the unit points in the figure are far apart. Figure 5d shows the reversible reflection band shifts upon alternately exposing N₂ and different concentrations of ethanol. We found that the stability of the ZIF-8 superstructure was poor. When the concentration of ethanol increased from 500 to 1000 ppm, the macrostructure and optical color were eroded, which depicts that the ZIF-8 superstructure lacks solvent resistance and repeatability.

In contrast, to demonstrate how PDMS coating supports excellent saturation, stability, and robustness, we studied the static and dynamic chemical sensing performance of ZIF-8@ PDMS superstructures. Figure 6a shows reflection spectra of the ZIF-8@PDMS superstructure during EtOH sensing. The primary reflection band at $\lambda = 700$ nm experiences a red-shift to 745 nm within 10 s after exposure to 500 ppm of ethanol vapors. Surprisingly, the narrower full width at half-maximum of the wavelength demonstrated higher optical saturation of the ZIF-8@PDMS than that of ZIF-8 superstructures. Also,

sensing of methanol, acetone, dichloromethane, and n-hexane was observed on the superstructure, which showed significant reflection band shifts of 44, 46, 49, and 49 nm, respectively (Figure S8). $\Delta\lambda$ and ΔR were summarized to demonstrate a clear chemical sensing performance (Table S2). Figure 6b shows the difference in the sensing response time and recovery time of the ZIF-8 superstructure calculated from time-resolved mean band reflections. The response times of methanol, ethanol, acetone, dichloromethane, and n-hexane sensing were 5.2, 10.5, 17.4, 13.5, and 40.0 s, respectively. The corresponding recovery times are 15.5, 5.0, 17.0, 7.5, and 38.5 s, respectively.

Figure 6c shows a clear separation of all six chemicals on the PCA plot, which indicated high sensitivity for the discrimination of the analytes. Figure 6d shows the reversible reflection band shifts upon alternately exposing the superstructure to N2 and different concentrations of ethanol. Quick response in only minor variations in reflectance ($\pm 0.5\%$ in R%) was obtained after 12 cycles of 500 ppm ethanol vapor exposure, suggesting great stability for chemical sensing. In addition, when the concentration of ethanol increased from 500 to 1000 ppm, the macrostructure and optical color remained unaltered, which demonstrated excellent stability and solvent resistance of the ZIF-8@PDMS superstructure compared with the ZIF-8 superstructure (Figure S9). Finally, we completely immersed ZIF-8 and ZIF-8@PDMS superstructures in liquid ethanol to observe the effect of PDMS nanocoating on the stability of the superstructure in normal conditions. In the experiment, two groups of superstructures were immersed in 1 mL ethanol solvents, the interval of optical photography was 10 s, and the distance from the drop of ethanol to the surface of the superstructures was \sim 1 cm. Figure S10 shows the film structure and color change of two groups of superstructures during the process of ethanol evaporation. We found that the structural colors of the two groups changed

from yellow-green to purple-red and then to yellow-green shortly after immersion in ethanol. However, the structure of ZIF-8 was quickly destroyed after immersion in ethanol. In contrast, the structure of the ZIF-8@PDMS superstructure remained stable during the whole immersion process, which further showed that the existence of PDMS nanocoating can improve the robustness of the self-assembled MOF superstructure and contribute to integrated application in optical communication.

3. CONCLUSIONS

In summary, we have demonstrated that robust and solventresistant MOF-based superstructures can be constructed by self-assembling ZIF-8 colloidal nanoparticles with monodispersity and shape homogeneity. Average size of ZIF-8 nanoparticles defined the reflection tunability in the whole visible range, and the optical properties were changed by the chemicals adsorbed in the micropores of the ZIF-8 nanoparticles. These characteristics should enable the development of self-assembled, MOF-based photonic crystals for sensing applications. In addition, we deposited PDMS nanocoating on the surface of the ZIF-8 superstructure to improve the robustness and solvent resistance. Static and dynamic sensing results demonstrated that the hierarchical pores endow the ZIF-8@PDMS superstructure with higher optical saturation and faster response in comparison to their counterparts configured with a ZIF-8 superstructure. These findings suggest that MOF crystals can be used for the self-assembly of longrange periodic superstructures, which is promising for the unambiguous detection of small molecules and linear homologues and is attractive for the on-demand design of sensor devices.

ASSOCIATED CONTENT

Supporting Information

The Supporting Information is available free of charge at https://pubs.acs.org/doi/10.1021/acsanm.4c00058.

Details of the experimental methods; SEM images of monodisperse ZIF-8 particles; optimization of the ZIF-8 superstructures by assembly concentration and evaporation temperature; AFM images of the self-assembled MOF superstructures; chemical sensing of the ZIF-8 and ZIF-8@PDMS superstructures; principal component (PCA) analysis of the ZIF-8 and ZIF-8@PDMS superstructures; dynamic sensing of ZIF-8 and ZIF-8@PDMS superstructures; and robust and solvent resistance of the ZIF-8@PDMS superstructure (PDF)

AUTHOR INFORMATION

Corresponding Author

Jianxi Liu — State Key Laboratory of Solidification Processing, MIIT Key Laboratory of Radiation Detection Materials and Devices, Center of Advanced Lubrication and Seal Materials, School of Materials Science and Engineering, Northwestern Polytechnical University, Xi'an 710072, P. R. China; orcid.org/0000-0002-6394-600X; Email: jianxiliu@nwpu.edu.cn

Authors

Zhihuan Li — State Key Laboratory of Solidification Processing, MIIT Key Laboratory of Radiation Detection Materials and Devices, Center of Advanced Lubrication and

- Seal Materials, School of Materials Science and Engineering, Northwestern Polytechnical University, Xi'an 710072, P. R. China; orcid.org/0000-0002-6637-9880
- Li Feng State Key Laboratory of Solidification Processing, MIIT Key Laboratory of Radiation Detection Materials and Devices, Center of Advanced Lubrication and Seal Materials, School of Materials Science and Engineering, Northwestern Polytechnical University, Xi'an 710072, P. R. China
- Gaohang Huo State Key Laboratory of Solidification Processing, MIIT Key Laboratory of Radiation Detection Materials and Devices, Center of Advanced Lubrication and Seal Materials, School of Materials Science and Engineering, Northwestern Polytechnical University, Xi'an 710072, P. R. China
- Jiayi Hao State Key Laboratory of Solidification Processing, MIIT Key Laboratory of Radiation Detection Materials and Devices, Center of Advanced Lubrication and Seal Materials, School of Materials Science and Engineering, Northwestern Polytechnical University, Xi'an 710072, P. R. China
- Chen Li State Key Laboratory of Solidification Processing, MIIT Key Laboratory of Radiation Detection Materials and Devices, Center of Advanced Lubrication and Seal Materials, School of Materials Science and Engineering, Northwestern Polytechnical University, Xi'an 710072, P. R. China
- Zhengze He State Key Laboratory of Solidification Processing, MIIT Key Laboratory of Radiation Detection Materials and Devices, Center of Advanced Lubrication and Seal Materials, School of Materials Science and Engineering, Northwestern Polytechnical University, Xi'an 710072, P. R. China
- Evgeniya Sheremet Research School of Chemistry & Applied Biomedical Sciences, Tomsk Polytechnic University, Tomsk 634050, Russia
- Yadong Xu State Key Laboratory of Solidification Processing, MIIT Key Laboratory of Radiation Detection Materials and Devices, Center of Advanced Lubrication and Seal Materials, School of Materials Science and Engineering, Northwestern Polytechnical University, Xi'an 710072, P. R. China; orcid.org/0000-0002-1017-9337

Complete contact information is available at: https://pubs.acs.org/10.1021/acsanm.4c00058

Author Contributions

§Z.L. and L.F. contributed equally to this work.

Notes

The authors declare no competing financial interest.

ACKNOWLEDGMENTS

The authors declare no conflict of interest. The authors thank the National Natural Science Foundations of China (52071270), the Research Fund of the State Key Laboratory of Solidification Processing (NPU) (2022-QZ-04), the Science Fund of Shandong Laboratory of Advanced Materials and Green Manufacturing (Yantai) (AMGM2023F03), the Russian Science Foundation grant (23-42-00081), and the National Key Research and Development Program of China (2023YFE0206300) for the financial support. The authors thank the Analytical & Testing Center of Northwestern Polytechnical University and Shanxi Materials Analysis and Research Center. All data are available in the main text or Supporting Materials.

REFERENCES

- (1) Sreekanth, K. V.; Das, C. M.; Medwal, R.; Mishra, M.; Ouyang, Q.; Rawat, R. S.; Yong, K. T.; Singh, R. Electrically Tunable Singular Phase and Goos—Hänchen Shifts in Phase-Change-Material-Based Thin-Film Coatings as Optical Absorbers. *Adv. Mater.* **2021**, 33, No. 2006926, DOI: 10.1002/adma.202006926.
- (2) Wang, Z.; Dai, C.; Zhang, J.; Wang, D.; Shi, Y.; Wang, X.; Zheng, G.; Zhang, X.; Li, Z. Real-Time Tunable Nanoprinting-Multiplexing with Simultaneous Meta-Holography Displays by Stepwise Nanocavities. *Adv. Funct. Mater.* **2022**, 32, No. 2110022, DOI: 10.1002/adfm.202110022.
- (3) Zheng, Y.; Wang, Z.; Liu, J.; Zhang, Y.; Gao, L.; Wang, C.; Zheng, X.; Zhou, Q.; Yang, Y.; Li, Y.; Tang, H.; Qu, L.; Zhao, Y.; Yang, C. Long-Lived Room Temperature Phosphorescence Crystals with Green Light Excitation. ACS Appl. Mater. Interfaces 2022, 14, 15706–15715.
- (4) Dai, C.; Li, Z.; Li, Z.; Shi, Y.; Wang, Z.; Wan, S.; Tang, J.; Zeng, Y.; Li, Z. Direct-Printing Hydrogel-Based Platform for Humidity-Driven Dynamic Full-Color Printing and Holography. *Adv. Funct. Mater.* **2022**, *n/a*, No. 2212053, DOI: 10.1002/adfm.202212053.
- (5) Xiao, Y.-H.; Gu, Z.-G.; Zhang, J. Vapor-assisted epitaxial growth of porphyrin-based MOF thin film for nonlinear optical limiting. *Sci. China: Chem.* **2020**, *63*, 1059–1065.
- (6) He, L.; Chen, Y.; Chen, S.; Wu, X.; Liu, J. Effects of Chlorella vulgaris on phosphorus release from ferric phosphate sediment by consecutive cultivations. *R. Soc. Open Sci.* **2022**, *9*, No. 211391.
- (7) Li, Z.; Liu, J.; Feng, L.; Liu, X.; Xu, Y.; Zhou, F.; Liu, W. Coupling tandem MOFs in metal-insulator-metal resonator advanced chemo-sieving sensing. *Nano Today* **2023**, *48*, No. 101726.
- (8) Meng, Z.; Wu, Y.; Zhang, S.; Wu, S. Sharp scattering spectra induced brilliant and directional structural colors. *Sci. China Mater.* **2021**, *64*, 420–429.
- (9) Zheng, J.; Chow, T. H.; Li, S.; Wang, J.; Shao, L. Electrophoretic Plasmonic Ink for Dynamic Color Display. *Adv. Opt. Mater.* **2021**, *9*, No. 2100091, DOI: 10.1002/adom.202100091.
- (10) Zhang, J.; Li, Q.; Dai, C.; Cheng, M.; Hu, X.; Kim, H. S.; Yang, H.; Preston, D. J.; Li, Z.; Zhang, X.; Lee, W. K. Hydrogel-Based, Dynamically Tunable Plasmonic Metasurfaces with Nanoscale Resolution. *Small* **2022**, *18*, No. 2205057, DOI: 10.1002/smll.202205057.
- (11) Kou, D.; Zhang, Y.; Zhang, S.; Wu, S.; Ma, W. High-sensitive and stable photonic crystal sensors for visual detection and discrimination of volatile aromatic hydrocarbon vapors. *Chem. Eng. J.* **2019**, 375, No. 121987.
- (12) Zhang, Y.; Fu, Q.; Ge, J. Photonic sensing of organic solvents through geometric study of dynamic reflection spectrum. *Nat. Commun.* **2015**, *6*, No. 7510.
- (13) Jian, Y.; Hu, W.; Zhao, Z.; Cheng, P.; Haick, H.; Yao, M.; Wu, W. Gas Sensors Based on Chemi-Resistive Hybrid Functional Nanomaterials. *Nano-Micro Lett.* **2020**, *12*, No. 71, DOI: 10.1007/s40820-020-0407-5.
- (14) Guo, L.; Lei, J.; Zhang, Y.; Duan, X.; Wang, X.; Zhang, Z.; Wei, Z.; Li, L.; Guo, Q.; Liu, X.; Ning, R.; Wang, J.; Hu, W.; Wu, W. MoS2/MXene pillared nanocomposite for ultrafast photonics applications. *Nanotechnology* **2022**, 33, No. 315701.
- (15) Liang, W.; Liqi, Z.; Zhicheng, X.; Fangfang, W.; Jianxin, C.; Baile, C. Investigation of low frequency noise-current correlation for the InAs/GaSb type-II superlattice long-wavelength infrared detector. *Opt. Quantum Electron.* **2022**, *54*, No. 286, DOI: 10.1007/s11082-021-03450-5.
- (16) Tian, Y.-B.; Tanaka, K.; Chang, L.-M.; Wöll, C.; Gu, Z.-G.; Zhang, J. Highly Efficient Light Helicity Detection of Enantiomers by Chiral Metal—Organic Framework Thin Films. *Nano Lett.* **2023**, 23, 5794—5801.
- (17) Avci, C.; De Marco, M. L.; Byun, C.; Perrin, J.; Scheel, M.; Boissière, C.; Faustini, M. Metal—Organic Framework Photonic Balls: Single Object Analysis for Local Thermal Probing. *Adv. Mater.* **2021**, 33, No. 2104450, DOI: 10.1002/adma.202104450.

- (18) Chen, S.; Bu, D.; Hu, Y.; Xiao, X.; Yang, D.; Ma, D.; Huang, S. Photonic Crystals with Tunable Lattice Structures Based on Anisotropic Metal—Organic Framework Particles and Their Application in Anticounterfeiting. *Adv. Photonics Res.* **2021**, 3, No. 2100246, DOI: 10.1002/adpr.202100246.
- (19) Liu, C.; Tong, Y. L.; Yu, X. Q.; Shen, H.; Zhu, Z.; Li, Q.; Chen, S. MOF-Based Photonic Crystal Film toward Separation of Organic Dyes. ACS Appl. Mater. Interfaces 2020, 12, 2816–2825.
- (20) Zhang, R.; Zhang, D.; Yao, Y.; Zhang, Q.; Xu, Y.; Wu, Y.; Yu, H.; Lu, G. Metal-Organic Framework Crystal-Assembled Optical Sensors for Chemical Vapors: Effects of Crystal Sizes and Missing-Linker Defects on Sensing Performances. ACS Appl. Mater. Interfaces 2019, 11, 21010–21017.
- (21) Fan, X.; Xu, M.; Liu, W.; Kuchmizhak, A.; Pattelli, L.; Li, Y.; Xu, H. Resolving Molecular Size and Homologues with a Self-Assembled Metal—Organic Framework Photonic Crystal Detector. *ACS Mater. Lett.* **2023**, *5*, 1703—1709.
- (22) Katayama, Y.; Kalaj, M.; Barcus, K. S.; Cohen, S. M. Self-Assembly of Metal-Organic Framework (MOF) Nanoparticle Monolayers and Free-Standing Multilayers. *J. Am. Chem. Soc.* **2019**, 141, 20000–20003.
- (23) Liang, W.; Ricco, R.; Maddigan, N. K.; Dickinson, R. P.; Xu, H.; Li, Q.; Sumby, C. J.; Bell, S. G.; Falcaro, P.; Doonan, C. J. Control of Structure Topology and Spatial Distribution of Biomacromolecules in Protein@ZIF-8 Biocomposites. *Chem. Mater.* **2018**, *30*, 1069–1077.
- (24) Pan, Y.; Liu, Y.; Zeng, G.; Zhao, L.; Lai, Z. Rapid synthesis of zeolitic imidazolate framework-8 (ZIF-8) nanocrystals in an aqueous system. *Chem. Commun.* **2011**, *47*, 2071–2073.
- (25) Avci, C.; Imaz, I.; Carne-Sanchez, A.; Pariente, J. A.; Tasios, N.; Perez-Carvajal, J.; Alonso, M. I.; Blanco, A.; Dijkstra, M.; Lopez, C.; Maspoch, D. Self-assembly of polyhedral metal-organic framework particles into three-dimensional ordered superstructures. *Nat. Chem.* **2018**, *10*, 78–84.
- (26) Avci, C.; Imaz, I.; Carne-Sanchez, A.; Angel Pariente, J.; Tasios, N.; Perez-Carvajal, J.; Isabel Alonso, M.; Blanco, A.; Dijkstra, M.; Lopez, C.; Maspoch, D. Self-assembly of polyhedral metal-organic framework particles into three-dimensional ordered superstructures. *Nat. Chem.* **2018**, *10*, 78–84, DOI: 10.1038/nchem.2875.
- (27) Ahmad, N.; Samavati, A.; Nordin, N. A. H. M.; Jaafar, J.; Ismail, A. F.; Malek, N. A. N. N. Enhanced performance and antibacterial properties of amine-functionalized ZIF-8-decorated GO for ultra-filtration membrane. *Sep. Purif. Technol.* **2020**, 239, No. 116554.
- (28) Japip, S.; Erifin, S.; Chung, T.-S. Reduced thermal rearrangement temperature via formation of zeolitic imidazolate framework (ZIF)-8-based nanocomposites for hydrogen purification. *Sep. Purif. Technol.* **2019**, 212, 965–973.
- (29) Pokhrel, J.; Bhoria, N.; Anastasiou, S.; Tsoufis, T.; Gournis, D.; Romanos, G.; Karanikolos, G. N. CO2 adsorption behavior of aminefunctionalized ZIF-8, graphene oxide, and ZIF-8/graphene oxide composites under dry and wet conditions. *Microporous Mesoporous Mater.* **2018**, 267, 53–67.
- (30) Hu, Y.; Kazemian, H.; Rohani, S.; Huang, Y.; Song, Y. In situ high pressure study of ZIF-8 by FTIR spectroscopy. *Chem. Commun.* **2011**, *47*, 12694–12696.
- (31) Jiang, M.; Cao, X.; Zhu, D.; Duan, Y.; Zhang, J. Hierarchically Porous N-doped Carbon Derived from ZIF-8 Nanocomposites for Electrochemical Applications. *Electrochim. Acta* **2016**, *196*, *699*–707.
- (32) Xu, J.; Shanshan, H.; Gang, H.; Jun, L.; Songwei, L.; Cher Hon, L.; Sui, Z.; Lu, S. Aqueous One-Step Modulation for Synthesizing Monodispersed ZIF-8 Nanocrystals for Mixed-Matrix Membrane. *ACS Appl. Mater. Interfaces* **2021**, *13*, 11296–11305, DOI: 10.1021/acsami.0c22910.
- (33) Kuang, M.; Wu, L.; Huang, Z.; Wang, J.; Zhang, X.; Song, Y. Inkjet Printing of a Micro/Nanopatterned Surface to Serve as Microreactor Arrays. ACS Appl. Mater. Interfaces 2020, 12, 30962—30971.
- (34) He, Y.; Bai, L.; Liu, B.; Duan, H.; Zhang, J. Construction of Quasi-Ordered Metal-Organic Frameworks Superstructures via

- Colloidal Assembly of Anisotropic Particles for Selective Organic Vapor Sensing. *Nanomaterials* **2023**, *13*, 2733.
- (35) Luo, W.; Zheng, Y.; Yan, J.; Chen, Y. Three-Dimensional Ordered Structures of Metal-Organic Frameworks for Carbon Tetrachloride Sensing and Comparative Study. *ChemistrySelect* **2019**, *4*, 3936–3939.
- (36) Yan, X.; Qu, H.; Chang, Y.; Pang, W.; Wang, Y.; Duan, X. Surface Engineering of Metal-Organic Framework Prepared on Film Bulk Acoustic Resonator for Vapor Detection. *ACS Appl. Mater. Interfaces* **2020**, *12*, 10009–10017.
- (37) He, S.; Chen, L.; Cui, J.; Yuan, B.; Wang, H.; Wang, F.; Yu, Y.; Lee, Y.; Li, T. General Way To Construct Micro- and Mesoporous Metal—Organic Framework-Based Porous Liquids. *J. Am. Chem. Soc.* **2019**, *141*, 19708—19714.
- (38) Li, Z.; Liu, J.; Yi, X.; Wu, W.; Li, F.; Zhu, Z.; Li, H.; Shi, J.; Xu, Y.; Zhou, F.; Liu, W. Metal-Organic Frameworks-Based Fabry-Perot Cavity Encapsulated TiO2 Nanoparticles for Selective Chemical Sensing. *Adv. Funct. Mater.* **2022**, 32, No. 2109541, DOI: 10.1002/adfm.202109541.
- (39) Tu, M.; Wannapaiboon, S.; Khaletskaya, K.; Fischer, R. A. Engineering Zeolitic-Imidazolate Framework (ZIF) Thin Film Devices for Selective Detection of Volatile Organic Compounds. *Adv. Funct. Mater.* **2015**, 25, 4470–4479.
- (40) Qin, Y.; Xie, J.; Liu, S.; Bai, Y. Selective methanol-sensing of SnS-supported ultrathin ZIF-8 nanocomposite with core-shell heterostructure. *Sens. Actuators, B* **2022**, *368*, No. 132230.
- (41) Luo, S.; Chen, R.; Wang, J.; Xie, D.; Xiang, L. Designed synthesis of ZnO/Pd@ZIF-8 hybrid structure for highly sensitive and selective detection of methane in the presence of NO₂. Sens. Actuators, B **2021**, 344, No. 130220.